# Lawrence Berkeley National Laboratory

**Title**
The mechanism for iron-catalyzed alkene isomerization in solution

**Permalink**
https://escholarship.org/uc/item/4xm3t787

**Author**
Sawyer, Karma R.

**Publication Date**
2009-01-06

# The mechanism for iron-catalyzed alkene isomerization

# in solution

*Karma R. Sawyer, Elizabeth A. Glascoe[†], James F. Cahoon, Jacob P. Schlegel and Charles B. Harris\**

Department of Chemistry, University of California, Berkeley, California 94720, and Chemical Sciences

Division Lawrence Berkeley National Laboratory, Berkeley, California 94720.

cbharris@berkeley.edu

**RECEIVED DATE (to be automatically inserted after your manuscript is accepted if required**

**according to the journal that you are submitting your paper to)**

[†] present address: Lawrence Livermore National Laboratory, mail stop  235, 7000 East Ave, Livermore, CA 94550

ABSTRACT.

Here we report nano- through microsecond time-resolved IR experiments of iron-catalyzed alkene isomerization in room-temperature solution. We have monitored the photochemistry of a model system, $Fe(CO)_4(\eta^2$-1-hexene)$, in neat 1-hexene solution. UV-photolysis of the starting material leads to the dissociation of a single CO to form $Fe(CO)_3(\eta^2$-1-hexene)$, in a singlet spin state. This CO loss complex shows a dramatic selectivity to form an allyl hydride, $HFe(CO)_3(\eta^3$-$C_6H_{11})$, via an internal C–H bond-cleavage reaction in 5–25 ns. We find no evidence for the coordination of an alkene molecule from the bath to the CO loss complex, but do observe coordination to the allyl hydride, indicating that it is the key intermediate in the isomerization mechanism. Coordination of the alkene ligand to the allyl hydride leads to the formation of the bis-alkene isomers, $Fe(CO)_3(\eta^2$-1-hexene)$(\eta^2$-2-hexene)$ and $Fe(CO)_3(\eta^2$-1-hexene)$_2$. Because of the thermodynamic stability of $Fe(CO)_3(\eta^2$-1-hexene)$(\eta^2$-2-hexene)$ over $Fe(CO)_3(\eta^2$-1-hexene)$_2$ (ca. 12 kcal/mol), nearly 100% of the alkene population will be 2-alkene. The results presented herein provide the first direct evidence for this mechanism in solution and suggest modifications to the currently accepted mechanism.

KEYWORDS. Catalytic iron-assisted alkene isomerization, time-resolved IR spectroscopy, metal-CO complexes

## I. Introduction

One of the most important roles of organometallic complexes is their frequent use as homogeneous catalysts in organic reactions.[1] Photoactivated $Fe(CO)_5$, which is used to catalyze alkene isomerization, is a particularly efficient catalyst, and as a result, it has been used by synthetic chemists for decades.[1-7] Numerous mechanistic studies have resolved the key intermediates in the isomerization reaction under a variety of conditions (gas- and solution-phase and low temperature matrices),[3,4,6-17] yet many questions remain about the mechanism in room-temperature solution, particularly concerning the role of high spin intermediates. Here we report on time-resolved infrared (IR) experiments performed on the nano- through the microsecond time-scales that answer the remaining questions and conclusively determine the mechanism in solution. We have also performed a computational investigation using density functional theory (DFT) modeling to explore steps in the reaction that are not experimentally observable. Our experimental results, coupled with the DFT analysis, give reason for a significant revision of the currently accepted mechanism.[13,14]

The most detailed mechanism for this reaction currently presented in the literature is based on time-resolved IR studies in the gas phase and is summarized in Scheme 1.[13,14] In the gas phase, UV-irradiation of $Fe(CO)_5$ leads to the dissociation of two CO ligands to form $^3Fe(CO)_3$.[9,11,18-20] It is hypothesized that $^3Fe(CO)_3$ coordinates a single 1-pentene molecule via a spin-allowed process to form $Fe(CO)_3$(1-pentene) (**B₁**).[13,14] The efficiency of the isomerization reaction may be due to the proposed triplet spin state of **B₁**, however, no study has explored how or why the high spin state accelerates the reaction.[9,11,18,20-22] Species **B₁** was not directly observed in the gas phase experiments, but was assumed to undergo an intramolecular C–H bond-cleavage reaction to form the allyl hydride species, $HFe(CO)_3(\eta^3\text{-}C_5H_9)$ (**C**) faster than the time resolution of the experiments (70 ns).[13,14] The authors propose that, in addition to the **B₁➔C** intramolecular rearrangement, **B₁** and its 2-pentene analog, **B₂**, react via a collision with a gaseous 1-pentene molecule to form a singlet bisalkene species (**D**), either $Fe(CO)_3$(1-pentene)₂ (**D₁**) or $Fe(CO)_3$(1-pentene)(2-pentene) (**D₂**).[13,14] Again, the authors were unable to observe the **B₁➔D** reaction because, at the experimentally accessible pressures of 1-pentene, this

reaction is slow relative to the **B₁→C** reaction. However, the rate of the **B₁→D** reaction in solution may be as fast, if not faster, than the internal rearrangement reaction to form **C**. Since neither of the key steps have been observed experimentally, significant questions remain about the mechanism. [13,14]

Here we investigate the mechanism for iron-catalyzed alkene isomerization in room-temperature solution. We cannot study the isomerization reaction directly with photoactivated $Fe(CO)_5$ because in solution irradiation of this complex with a single pulse of UV light leads to the dissociation of a single CO to form $Fe(CO)_4$ and not the active metal catalyst, $^3Fe(CO)_3$.[23] We circumvent this challenge by using $Fe(CO)_4(\eta^2$-1-hexene) (**A**) as a model system. Irradiation of this complex with a single 266-nm laser pulse leads to the dissociation of a single CO to form $Fe(CO)_3(\eta^2$-1-hexene) (**B₁**), the first intermediate in the isomerization reaction (Scheme 1).[11,13,14,24] We have investigated the reactivity of **B₁** in neat 1-hexene solution in order to directly monitor the rates and mechanism for the formation of **C** and **D**.

Recently, Glascoe et al. performed a similar experiment on a picosecond time-scale and found that after 266-nm excitation of **A** a single CO is dissociated to form **B₁** within a few ps.[11] Species **B₁** does not react on the time-scale of the ultrafast experiments ($\tau < 5$ ns) and neither **C** nor **D** was observed, presumably because the **B₁→C** and **B₁→D** reactions occur on a longer time-scale.[11] We have monitored this reaction using nano- through the microsecond time-resolved IR spectroscopy in order to observe these key steps.

## II. Methods

### A. Sample preparation: Synthesis of $Fe(CO)_4(\eta^2$-1-hexene) (A)

$Fe(CO)_4(\eta^2$-1-hexene) (**A**) was prepared by a modified version of a published procedure.[11,25] A 1.7-g (0.0045 mol) portion of $Fe_2(CO)_9$ (Sigma-Aldrich) and 10 mL (0.08 mol) of 1-hexene (Sigma-Aldrich) were combined and stirred in the dark under a $N_2$ atmosphere for ca. 20 hours. This mixture was distilled and fractionally condensed for ca. 30 hours. The identity of the sample was verified with static FTIR spectroscopy. The sample was diluted in a small excess of 1-hexene and stored at –80 $^o$C. Dilute solutions were prepared in 1-hexene. Because the contaminants precipitate out of solution at low

4

temperature, solutions were prepared by decanting a small aliquot of the sample while it was held in dry ice. For experiments, a 0.5-mL aliquot of **A** was diluted to 75 mL with 1-hexene (Sigma-Aldrich) to give a final sample concentration of a few millimolar. Static FTIR spectra were taken prior to experiments to ensure sample purity. The sample is stable when exposed to air under ambient conditions for ca. 24 hours.

## B. Nanosecond and microsecond FTIR spectroscopy

The experimental setup of the step-scan FTIR apparatus has been described in detail elsewhere.[26,27] For experiments in the 1700–2100 $cm^{-1}$ region with a spectral resolution of ca. 4 $cm^{-1}$, an HgCdTe PV detector KMPV8-1-J2 (fwhm = 37 ns, RC decay of AC amplifier = 1.4 ms) was employed. AC-coupled and DC-coupled interferometric signals were simultaneously acquired by a 40-MHz, 12-bit digitizer (model PAD 1232). Samples were photolyzed with 25-ns pulses of the fourth harmonic of a Nd:YAG laser (DCR2A, GCR-3 optics) at 266-nm. Photolysis light was aligned in a nearly collinear geometry (10°) with the infrared beam. To prevent scattered 266-nm light from reaching the interferometer and detector optics, AR-coated Ge plates (International Scientific, 95% transmittance) were placed in the openings of the interferometer and detector compartments. Data acquisition was triggered by a small fraction of the photolysis laser pulse detected with an EG&G Silicon photodiode (SGD-444). A sample cell that is similar to the one used by Glascoe et al. in their ultrafast experiments was used.[11] Data was typically averaged over 15 laser-induced decays recorded for each mirror position of the step-scan apparatus and 5–10 full time-resolved step-scan experiments were performed on each sample to ensure reproducibility and allow for statistical analysis of data. Typically, changes in optical density of $5\times10^{-5}$ were resolvable in these experiments.

Time-scales for reactant and product evolution were determined by fitting the peak area, plotted as a function of time, to a sum of exponentials with the Levenberg-Marquart method. All errors correspond to a 95% confidence interval.

## C. Density functional theory calculations

Density functional theory (DFT) calculations have been used to model the isomerization reaction because they have been shown to be reliable for calculating energies, structures and frequencies for transition-metal complexes.[11,23,28-33] Whenever possible the shortest chain alkene was used in order to minimize computational expense. The same species labels (**A**-**D**) were used for both experiment and theory regardless of whether the alkene chain was hexene or a shorter alkene (butene or ethene), respectively. For example, species **C** corresponds to $HFe(CO)_3(C_6H_9)$ in the experiments, but corresponds to $HFe(CO)_3(C_4H_7)$ in the DFT calculations. Shortening the alkene ligand to reduce computational expense has been done in studies of similar systems and is not expected to effect the mechanistic results.[11,13,14,34]

All calculations were performed with Gaussian03 program package and utilized Becke's 1988 exchange functional together with the Perdew 1986 correlation functional (BP86).[35,36] The 6-31+g* basis set was used for carbon and oxygen atoms; the 6-31+g** basis set was used for hydrogen atoms; and the LANL2DZ basis set was used for iron atoms.[37-39] The LANL2DZ effective core potential were used for iron atoms to account for relativistic effects.[40] Transition states were calculated using the combined synchronous transit-guided and quasi-Newton (STQN) method.[41,42] All transition states were verified by following the appropriate eigenvectors, i.e. those eigenvectors corresponding to the imaginary frequency, to their interconnected stationary points. The reported energies for fully optimized molecular structures correspond to zero-point corrected electronic energies. The Cartesian coordinates for all fully optimized molecular geometries are provided in the SI. Frequency calculations were done for all local minima and saddle points, and have not been scaled.[24]

Since species $\mathbf{B_1}$ has been proposed to be most stable in the triplet spin state, we have modeled the formation of **C** from the triplet potential of $Fe(CO)_3(\eta^2\text{-1-butene})$ ($\mathbf{B_1}$). One-dimensional slices of ground singlet ($S_0$) and triplet ($T_1$) potential energy surfaces were calculated by performing successive partial geometry optimizations and energy calculations in the triplet and singlet spin states of $\mathbf{B_1}$ at fixed distances between the iron and the γ-hydrogen (ca. 1.5 to 4 Å). This method is qualitatively effective at describing the dynamics of spin-forbidden reactions in transition-metal compounds, but the one-

dimensional slices of the potential energy surfaces calculated using this method are approximate since the true reaction pathways have high dimensionality in phase space.[30,43] The partial optimization calculations were also performed using the B3LYP[21,44,45] functional to test their accuracy in comparison to experiment,[29,34,46-48] and these results are presented in the SI. We have also performed the calculations of slightly different starting geometries of $B_1$ to verify the location of the crossing point. These calculations are discussed further in the SI. Transition state calculations were performed to identify the barriers to forming all **C** isomers identified by Cedeno et al. from the singlet forms of **B** and from the isomers of **C** identified by Cedeno et al.[34]

**III. Experimental Results: Nano- through microsecond time-resolved IR spectroscopy of Fe(CO)$_4$(1-hexene) in 1-hexene solution**

Nano- and microsecond time-resolved IR spectra of **A** in neat 1-hexene solution after laser irradiation at 266 nm are presented in Figures 1a and 1b, respectively. Table 1 shows peak assignments and the dynamics of all features. There are six features observed in Figure 1a—three negative peaks, assigned to **A** (1977, 2000 and 2078 cm$^{-1}$), two strong positive peaks centered at 1990 and 2058 cm$^{-1}$ and a small positive peak centered at 1930 cm$^{-1}$. All of the positive features are discernible at 25 ns and do not have dynamics between 25 ns and 1 μs. The large positive peaks at 1990 and 2058 cm$^{-1}$ are assigned to the antisymmetric and symmetric carbonyl stretches of **C**, respectively. The peak assignments are made on the basis of literature assignments and DFT-calculated CO stretching frequencies (Table 1).[11,16] The spectra in Figure 1a are noticeably different from the spectra of the same system measured by Glascoe et al. on the picosecond time-scale, which showed intense $B_1$ absorptions (1931 and 2031 cm$^{-1}$), but no peaks corresponding to **C**.[11] By 25 ns the features assigned to $B_1$ are no longer observable; instead, the **C** peaks have grown in, showing that $B_1$ has rearranged to form **C** on a time-scale of 5–25 ns.[11] Assuming that the oscillator strengths of the analogous CO stretching modes of $B_1$ and **C** are similar, the absence of $B_1$ peaks indicates that the equilibrium between $B_1$ and **C** favors species **C**.

In the spectra measured on a microsecond time-scale (Figure 1b), a new absorption at 1969 cm$^{-1}$ is observed and assigned to either Fe(CO)$_3$($\eta^2$-1-hexene)$_2$ ($D_1$) or Fe(CO)$_3$($\eta^2$-1-hexene)($\eta^2$-2-hexene)

($D_2$) on the basis of the literature values and DFT-calculated CO stretching frequencies (Table 1).[11,16,17,49] Additionally, the peaks labeled **C** decay on the microsecond time-scale. Kinetics plots for the **C** and **D** peaks are displayed in Figure 2 and are both well fit to a biexponential function (solid red line). Figure 2 also shows a single exponential fit to the data (dashed blue line). The single exponential does not fit the data adequately as it is not able to capture the early time dynamics. The biexponential fit to the data shows that the **D** peak grows in with fast rise time of $22 \pm 2$ μs and a slow rise time of $158 \pm 5$ μs. Similarly, the intensities of **C** peaks decay with an average fast decay time of $16 \pm 2$ μs and average slow decay time of $138 \pm 7$ μs. The biexponential dynamics of the **C** and **D** peaks suggest that **C** is reacting to form both isomers of **D**, i.e. $Fe(CO)_3(\eta^2\text{-1-hexene})_2$ (**D$_1$**) and $Fe(CO)_3(\eta^2\text{-1-hexene})(\eta^2\text{-2-hexene})$ (**D$_2$**).[50] However, we do not expect to be able to distinguish between species **D$_1$** and **D$_2$** by IR spectroscopy since the CO modes are expected to be nearly identical for the two isomers (Table 1). Species **D** is predicted to have two additional peaks at 2048 cm$^{-1}$ and 1977 cm$^{-1}$.[11] The former is a small shoulder of the 2058 cm$^{-1}$ peak centered at 2045 cm$^{-1}$ and the latter is masked by the parent bleach at 1977 cm$^{-1}$.[51] The intensity of the bleach at 1977 cm$^{-1}$ decreases with a fast time constant of $28 \pm 6$ μs and a slow time constant of $170 \pm 45$ μs, but the other parent bleaches (2078 and 2000 cm$^{-1}$) do not have dynamics on the microsecond time-scale. Therefore, we attribute the dynamics of the parent bleach at 1977 cm$^{-1}$ to the dynamics of an overlapping peak assigned to **D**.

The small peak centered at 1930 cm$^{-1}$ is assigned to an alkyl-solvated form of $Fe(CO)_3(\eta^2\text{-1-hexene})(alkyl)$ (**E**), solvated either by the alkyl portion of the 1-hexene ligand or the alkyl portion of a token ligand from the bath. We have performed control experiments of **A** in solution with neat cyclohexane and found a similar species.[52] The **E** peak does not have dynamics out to 500 μs indicating that it is a side-product to the iron-assisted alkene-isomerization reaction. Species **E** is not expected to be stable since alkane ligands generally interact weakly with coordinatively unsaturated transition-metal complexes. Ultimately, **E** will either reform **A** by collision with a carbonyl group, dimerize after collision with another metal complex or enter the catalytic cycle via rearrangement to **C** or **D**.[53] The

8

lifetime of **E** is limited by the rate of diffusion and weak binding strength of the saturated alkane, and thus, **E** is expected to decay on the micro- through millisecond time-scale.[33,54]

The high selectivity to form **D** from **C** rather than from **B₁** shows that the barrier of the **B₁→D** reaction is significantly greater than barrier to the **B₁→C** reaction, implying that the **C→D** reaction does not proceed through a **B₁** intermediate as predicted by past gas phase work (Scheme 1). This is further supported by the correlation between the dynamics of the **C** and **D** peaks. Moreover, the results suggest that **C** is the key intermediate in the isomerization reaction. If the reaction proceeds through **C**, shifting the location of the double bond to form either isomer of **D** is expected to be facile since the $\eta^3$-bound ligand on **C** is a transitional structure between a 1-hexene and a 2-hexene ligand.[14,17,25]

## IV. Results and Discussion

The experimental results presented above have been analyzed in the context of DFT calculations to elucidate the details of the isomerization mechanism that are not apparent from the experiments alone. This section is divided into three parts. In part A, we present the details of the **B→C** reaction, specifically the role of the transients in the $T_1$ state; in part B, we discuss the mechanism for the formation of **D₁** and **D₂** in light of the biexponential dynamics of the **C** and **D** peaks and the high barrier to the **B₁→D** reaction. On the basis of this combined experimental and computational study, we present a novel mechanism for iron-catalyzed alkene isomerization in Scheme 3.

### A. Mechanism for the formation of HFe(CO)₃($\eta^3$-C₄H₇) (C)

The experimental results imply an isomerization mechanism that is different from the mechanism presented in the literature (Scheme 1).[13] In solution, **B₁** undergoes an internal C–H bond activation reaction to form **C** on an early nanosecond time-scale ($\tau$ = 5–25 ns), but does not coordinate a second alkene from the bath to form **D**. It has been proposed that this selectivity is due to the high spin state of $^3$**B₁**.[11] Additionally, many authors have proposed that the triplet spin state of **B₁** contributes to the extraordinary efficiency of the isomerization reaction.[9,18,20,22,55] We have performed detailed DFT calculations to test this hypothesis and to identify the role of the ground triplet state in the formation of **C**. Unfortunately, an explicit, time-dependent simulation of the system is not computationally feasible

9

because the dynamics following photolysis involve multiple potentials. Furthermore, a precise calculation of spin-orbit coupling is necessary to accurately assess the spin-forbidden dynamics. Instead, one-dimensional sections of the relevant potential energy surfaces have been used to offer a qualitative picture for the dynamics of the system. These results lend considerable insight to the isomerization mechanism when they are analyzed in the context of the experimental results.

Figure 3 shows the energy of the both the ground singlet ($S_0$) and triplet ($T_1$) potential energy surfaces plotted as a function of the Fe–γH distance, shown in red and blue, respectively. These potentials were calculated by fixing the Fe–γH distance and allowing the remaining degrees of freedom in the system to fully optimize. Identical calculations were performed with a B3LYP functional to determine if the BP86 functional led to artificially stable singlet states. The calculations performed with the B3LYP functional, (refer to SI) do not agree with our experimental results or previously published experimental work because the calculations predict that the allyl hydride complex (**C**) is less energetically stable than the lowest energy form of the CO-loss complex (**B**).[8,9,11,13,14,16,17,34]

The triplet curve in Figure 3 shows that $^3$**B$_1$** is most stable with a Fe–γH distance of ca. 3.3 Å and increasing or decreasing that bond distance results in a rise in energy. The singlet curve shows two local minima along the Fe–γH coordinate at Fe–γH distances of 3.4 Å and 1.8 Å, **B$_1$**\* and **B$_1$**, respectively. The fully optimized structures for these local minima are shown in Figures 4. The structures of $^3$**B$_1$** and **B$_1$**\* (Figures 4a-4b) are nearly identical; the γ-H in $^3$**B$_1$** and **B$_1$**\* does not interact with the metal center and is bound only to the alkene moiety. Furthermore, these structures are significantly different from the **B$_1$** structure in Figure 4c that is discussed in detail below.

Figure 3 shows that the $S_0$ and $T_1$ surfaces are nearly isoenergetic in the vicinity of the $^3$**B$_1$** and **B$_1$**\* local minima. Since the $^3$**B$_1$** and **B$_1$**\* are energetically and structurally similar, we expect that there is crossing point in the vicinity of these minima and that $^3$**B$_1$** is a short-lived structure. While $S_0$ and $T_1$ are close in energy at long Fe–γH distances, when the distance decreases to less than 3 Å, the $S_0$ potential is lower in energy, suggesting that a spin-crossover to $S_0$ is thermodynamically favorable. These calculations are in agreement with past experimental work that showed that the allyl hydride complexes

are more thermodynamically stable than the CO loss structures.[8,9,11,13,14,16,17,34] Species $^3\mathbf{B_1}$ undergoes a spin crossover from $T_1$ to $S_0$ to form $\mathbf{B_1^*}$,[43,56] which is able to form a complex with an M–H–C agostic bond between the Fe atom and the $\gamma$H on the alkene moiety, species $\mathbf{B_1}$ (Figure 4c). The M–H–C agostic interaction stabilizes the complex by more than 8 kcal/mol. Species $\mathbf{B_1}$ is distinctly different from $\mathbf{C}$, the allyl hydride complex, and can be thought of as an internally solvated form of the CO loss complex. Because this agostic interaction stabilizes the coordinatively unsaturated metal center, $\mathbf{B_1}$ is the most thermodynamically stable structure of $Fe(CO)_3(\eta^2\text{-1-butene})$. Agostic M–H–C bonds are common in organometallic complexes and have been proposed to stabilize coordinatively unsaturated transients to such an extent that further solvent coordination is not necessary.[28,57] We were not able to identify a triplet structure with an agostic M–H–C, most likely because coordinatively unsaturated triplet metal centers do not interact favorably with saturated C–H bonds.[30,31,58] The other singlet forms of $Fe(CO)_3(\eta^2\text{-1-alkene})$, such as $\mathbf{B_1^*}$, are higher in energy than $^3\mathbf{B_1}$, and therefore, it is only thermodynamically favorable to form $\mathbf{B_1}$. Figure 4 also shows the 2-alkene isomer, $Fe(CO)_3(\eta^2\text{-2-butene})$ ($\mathbf{B_2}$), in which there is an agostic interaction between the $\alpha$C–H bond and the iron atom. Species $\mathbf{B_2}$ is nearly isoenergetic with $\mathbf{B_1}$.

Many authors argue that $Fe(CO)_3(\eta^2\text{-alkene})$ is most stable in the triplet spin state.[8,9,11,16,17] Our DFT calculations are in good agreement with this prediction; $^3\mathbf{B_1}$ is more energetically stable than the analogous singlet complex, $\mathbf{B_1^*}$ (see Table 2 and Figure 3). However, our calculations also show evidence for a self-solvated form of $Fe(CO)_3(\eta^2\text{-alkene})$ ($\mathbf{B_1}$), which is structurally different and more thermodynamically stable than $^3\mathbf{B_1}$. The calculated CO modes for $\mathbf{B_1}$ and $^3\mathbf{B_1}$ (Table 1) are both in reasonable agreement with experiment[11] given the accuracy of DFT calculations.[43] As a result, we cannot distinguish between the structures using their calculated CO stretching frequencies alone. Transition state calculations, discussed below, show that $\mathbf{B_1}$ will react to form $\mathbf{C}$ on a nanosecond time-scale, in agreement with experiment.[11] In light of these results, we expect that the peaks assigned to

Fe(CO)$_3$($\eta^2$-1-hexene) (**B$_1$**) observed on the picosecond time-scale are due to the singlet species (**B$_1$**) and not the triplet ($^3$**B$_1$**).[11]

Species **B$_1$** is structurally similar to the facial-endo isomer of **C** (**C$_{endo}$**) (Figure 4), though the Fe–γH bond distance is slightly shorter in **C$_{endo}$** and the hydrogen is not coordinated to the alkene ligand, suggesting that **B$_1$** is an intermediate structure between $^3$**B$_1$** and **C$_{endo}$**. We have performed a fully optimized transition state calculation for the **B$_1$**→**C$_{endo}$** reaction and found that the barrier is 3.7 kcal/mol and the reverse reaction barrier is 6.6 kcal/mol (Table 2). The calculated barrier for the **B$_2$**→**C$_{endo}$** reaction is 4.5 kcal/mol. These barriers correspond to a time-scale of pico- to nanoseconds for the formation of **C$_{endo}$** from **B$_1$**, in agreement with the experimental results.[59]

We have also performed transition state calculations to determine the barrier to **B**→**C** reaction for the other isomers of **C** (i.e. **C$_{endo}$** and **C$_{mer}$**; see Figure 4f-4g), that have been identified by Cedeno et al (Scheme 2 and Table 2). In agreement with Cedeno's work, we found that the **C$_{endo}$** and **C$_{exo}$** structures are more thermodynamically stable than the **C$_{mer}$** structure. [34] However, while **C$_{exo}$** is the most thermodynamically stable isomer, the barrier to the **B$_1$**→**C$_{exo}$** reaction is nearly an order of magnitude higher than the barrier to the **B$_1$**→**C$_{endo}$** reaction, indicating that only the **C$_{endo}$** isomer is formed directly from **B$_1$** on the early nanosecond time-scale. On a longer time-scale (ca. 500 nanoseconds), **C$_{endo}$** isomerizes to **C$_{exo}$** via **C$_{mer}$** and/or **B$_2$** intermediates, as shown in Scheme 2. On this longer time-scale all of the **B** and **C** isomers on the S$_0$ potential will be in equilibrium, but since the **C$_{exo}$** and **C$_{endo}$** structures are the most thermodynamically stable, we expect that the equilibrium favors them, in agreement with previous DFT work and the spectra in Figure 1.[34,60] Note that the spectral resolution of our experiments does not allow us to distinguish between the CO stretching modes of the different **C** isomers, These results are also in qualitative agreement with low temperature studies of Fe(CO)$_4$($\eta^2$-propene) that found that **B$_1$** thermally converts to one of the **C** isomers at 5 K and the other at 50 K.Barnhart, 1992 #3102}

Scheme 2 shows the equilibrium between the different isomers of **B** and **C**, in which the hydrogen (red) is migrating between the α- and γ-carbons on the alkene ligand and the double bond is moving

between 2-butene and 1-butene locations. Previous low-temperature $^1$H-NMR studies of the $\eta^3$-propyl analog of **C** provide further support for this type of reversible 1,3-hydrogen migration in the system. Moreover, the study suggests the existence of agostic structures, akin to $\mathbf{B_1}$ and $\mathbf{B_2}$.[8] Our DFT results illustrate that the only agostic structures are in the singlet spin state ($\mathbf{B_1}$ and $\mathbf{B_2}$), providing further evidence that $\mathbf{^3B_1}$ is not directly involved in the isomerization process. For clarity, hereafter the **C** label corresponds to the facial-endo isomer.

## B. Mechanism for the formation of Fe(CO)$_3$($\eta^2$-hexene) (D)

We hypothesize that species **C** is the key intermediate in the isomerization mechanism.[11,14,17,25] In the following section, we use DFT modeling and basic kinetic analysis to elucidate the reactivity of **C** on the microsecond time-scale.

### 1. Analysis of biexponential dynamics

The spectra in Figure 1b show that **C** decays to form **D** on a microsecond time-scale. The kinetic traces of the **C** and **D** peaks, shown in Figure 2, are well fit to biexponential functions giving an average fast time constant of 20 μs and an average slow time constant of 150 μs. These biexponential kinetics imply that **C** reacts to form to two isomers of **D** via two different pathways, $\mathbf{C} \rightarrow \mathbf{D_1}$ and $\mathbf{C} \rightarrow \mathbf{D_2}$. However, on the basis of the experiments alone we cannot determine which of these pathways has the lower barrier. We have used basic kinetic analysis of the parallel $\mathbf{C} \rightarrow \mathbf{D_1}$ and $\mathbf{C} \rightarrow \mathbf{D_2}$ pathways coupled with DFT calculated energies of **C** and **D** to elucidate the details of the reactions.

Figure 5 shows the DFT-calculated structures of $\mathbf{D_1}$ and $\mathbf{D_2}$ and the relative structural parameters for both complexes are presented in Table 3. Structurally, the only significant difference between $\mathbf{D_1}$ and $\mathbf{D_2}$ is the location of the double bond on the alkene ligand. Similarly, the calculated CO stretching modes of $\mathbf{D_1}$ and $\mathbf{D_2}$ are nearly identical and are in excellent agreement with the experimentally observed peaks (Table 1). Despite the structural similarities between $\mathbf{D_1}$ and $\mathbf{D_2}$, DFT calculations indicate that there is a significant energetic difference between them (Table 2).[61] Most notably, species $\mathbf{D_2}$ is ca. 10 kcal/mol lower in energy than **C**, while species $\mathbf{D_1}$ is slightly higher in energy than **C**.

13

These results suggest that there should be an equilibrium between $\mathbf{D_1}$ and $\mathbf{C}$, and that the $\mathbf{C} \rightarrow \mathbf{D_2}$ reaction is irreversible ($\Delta E$ = 12.2 kcal/mol).

$$C + alkene \underset{k_{-1}}{\overset{k_1}{\leftrightarrow}} D_1$$

and

$$C + alkene \overset{k_2}{\rightarrow} D_2$$

The rate equations for $\mathbf{C}$ and $\mathbf{D}$ for these parallel reactions are

$$\frac{d[C]}{dt} = k_1[D_1] - k[C] \quad (1)$$

and

$$\frac{d[D]}{dt} = -k_1[D_1] + k[C] \quad (2)$$

where $k = (k_{-1} + k_2)$ and [D] = [D$_1$]+[D$_2$].

According to equations (1) and (2), we would expect to observe a biexponential decay of the $\mathbf{C}$ peaks and a corresponding biexponential rise of the $\mathbf{D}$ peaks, assuming that the CO stretching modes of the $\mathbf{D}$ peaks are identical within the spectral resolution of our experiment. This prediction is in excellent agreement with the kinetics that we observe. The fast rate constant corresponds to the time it takes to establish an equilibrium between $\mathbf{C}$ and $\mathbf{D_1}$ ($k_1$) and the slow rate constant corresponds to the irreversible $\mathbf{C} \rightarrow \mathbf{D_2}$ reaction ($k = k_{-1} + k_2$). In other words, the equilibrium between $\mathbf{C}$ and $\mathbf{D_1}$ is established in 20 µs, but because $\mathbf{C}$ and $\mathbf{D_1}$ are nearly isoenergetic, once the equilibrium has been established, there is still population of $\mathbf{C}$ available to react via the slow pathway to form $\mathbf{D_2}$. This mechanism is presented in Figure 5.[59] Note that if we neglect the $\mathbf{D_1} \rightarrow \mathbf{C}$ back reaction, we would expect to observe a single exponential decay of the $\mathbf{C}$, and a corresponding single exponential rise of the $\mathbf{D}$ peaks with rate constants of ($k_1 + k_2$).

If $\mathbf{D_2}$ is formed via the fast pathway so that $k_2 > k_1$, the decay of $\mathbf{C}$ will be a single exponential because the $\mathbf{C} \rightarrow \mathbf{D_2}$ reaction will be completed before the $\mathbf{C} \rightarrow \mathbf{D_1}$ occurs.[59,62] The $\mathbf{C} \rightarrow \mathbf{D_2}$ reaction would

be ~90% complete within 45 μs,[59] and there would be no substantial back reaction since $D_2$ is considerably more stable than $C$. As a result, there would not be a significant population of $C$ remaining to react via slower pathway to form $D_1$. Therefore if the $C \rightarrow D_2$ reaction is faster than the $C \rightarrow D_1$ reaction, we would expect to observe a single exponential decay of the $C$ peaks and a corresponding single exponential rise of the $D$ peak due to species $D_2$, but no observable formation of species $D_1$.[59] The dashed blue line Figure 2 shows a single exponential fit to the experimental data. The single exponential function gives a poor fit to the data since it does not capture the dynamics before ca. 50 μs.

Using simple transition state theory to estimate the barriers from the experimentally observed time constants ($k = 1/\tau$), we find that the barrier for the $C \rightarrow D_1$ pathway is 1.2 kcal/mol lower in energy than the barrier to the $C \rightarrow D_2$ pathway.[62] The DFT-calculated molecular structure of $C$ gives qualitative insight into the reason for the difference between the barriers (Table 3). The $\alpha$C on the alkene ligand is slightly closer than the $\gamma$C to the metal center in $C$. The minor asymmetry in the allyl hydride structure, which is observed for all of the $C$ isomers (Table 3), suggests that there is a slightly lower barrier to forming a structure with 1-alkene ligand compared to the 2-alkene species. Note that we cannot distinguish which $C$ isomer reacts to form $D$ or if the $C$ isomers react differently in the $C \rightarrow D$ reaction. The DFT calculated barriers (Scheme 2) indicate that conversion between the $C$ isomers occurs on a nanosecond time-scale, and thus we do not expect to be able to observe any of the related dynamics on the time-scale of the $C \rightarrow D$ reaction. Furthermore, we are unable to distinguish between the CO stretching modes of the different $C$ isomers by IR spectroscopy (Table 1).

## 2. $HFe(CO)_3(\eta^3\text{-}C_6H_9) \rightarrow Fe(CO)_3(\eta^2\text{-}C_6H_{10})_2$ ($C \rightarrow D$): Associative vs. Dissociative

One of primary goals of this work was to experimentally determine the mechanism for forming $D$ in solution phase. The $C \rightarrow D$ reaction can be thought of as an intramolecular ligand substitution reaction in which the hydrogen bound to the metal center in $C$ is replaced by an alkene ligand from the bath to form $D$. Ligand substitution reactions are generally described using the either associative or dissociative mechanisms. In the context of this work, a dissociative mechanism does not correspond to the full dissociation of the hydrogen from the metal complex, but instead corresponds to a step-wise mechanism

15

in which the hydrogen is dissociated from the metal center in **C** and re-coordinates to the alkene moiety to form **B₁**. Species **B₁** is then solvated by an alkene molecule from the bath to form **D**. In contrast, the associative mechanism corresponds to a direct solvation of **C** by an alkene to form **D** so that the transfer of the hydrogen from the metal to the alkene and the solvation of the metal center happens concomittantly.[63] Previous gas phase studies have proposed a dissociative mechanism in which the triplet form of **B₁** (³**B₁**) is an intermediate in the **C➔D** reaction.[13,14] However, the authors were not able to observe the **B₁➔D** reaction, and therefore, were not able to rule out an associative mechanism.[13,14] We have already established that ³**B₁** is extremely short-lived, if it is formed at all (Figure 3), and thus, ³**B₁** cannot be solvated to form **D₁** as is predicted in Scheme 1.[64] However, the singlet form of **B₁** that is stabilized by a M–H–C agostic interaction is observable on the pico- through early nanosecond time-scales, and questions still remain about whether this singlet transient is an intermediate in the **C➔D** reaction.[11]

This work provides direct experimental evidence that **B₁** is not an intermediate in the **C➔D** reaction. The **B₁➔D** reaction is not observable on a pico- through microsecond time-scales,[11] indicating that the barrier to this reaction is considerably higher than the barrier to the **B₁➔C** reaction. If the barrier to the **B₁➔D** reaction were lower, we would observe **D** peaks on the pico- through the nanosecond time-scales since both **D** isomers are thermodynamically stable. Additionally, we see no evidence for **B₁** peaks past 25 ns (Figure 1). Thus, if **B₁** were an intermediate in the **C➔D** rearrangement, it would have to be under steady-state conditions, i.e. the concentration of **B₁** would have to remain sufficiently low so that its dynamics are not observable. In order for **B₁** to be under steady-state conditions, the **B₁➔D** reaction would have to be fast relative to the **B₁➔C** reaction.[59] Our experiments show the opposite trend, providing direct experimental evidence that **B₁** is not an intermediate in the **C➔D** reaction. However, we cannot exclude the possibility that there is a different short-lived intermediate in the reaction that is so short-lived that it is not observable.

This mechanism, summarized in Scheme 3, is different from the gas phase mechanism in Scheme 1. The most notable difference between the mechanisms is that in Scheme 3 **B₁** is not an intermediate in

the **C→D** rearrangement. While this mechanism is markedly different from the gas phase mechanism, the data presented in the gas phase studies do not preclude the mechanism that we propose. The dynamics of **B₁** was not observed in that work, and thus their data supports either mechanism. In contrast, the data presented herein provide the first direct experimental evidence that in the solution phase **B₁** is not an intermediate in the **C→D** reaction.[13,14]

## V. Conclusion

On the basis of this analysis, we present a novel mechanism for iron-catalyzed alkene isomerization, shown in Scheme 3. UV irradiation of $Fe(CO)_4(\eta^2\text{-1-hexene})$ (**A**) leads to the dissociation of a single CO to form $^3Fe(CO)_3(\eta^2\text{-1-hexene})$ ($^3$**B₁**), which undergoes a spin-crossover process on the sub-picosecond time-scale to form $Fe(CO)_3(\eta^2\text{-1-hexene})$ (**B₁**). The **B₁→D₁** reaction does not occur, and instead **B₁** reacts to form **C** via an internal C–H bond cleavage process in 5–25 ns. Species **C** is solvated by a 1-hexene molecule from the bath to form $Fe(CO)_3(\eta^2\text{-1-hexene})_2$ (**D₁**) in ca. 20 μs. Species **C** and **D₁** are nearly isoenergetic and, as a result, are in equilibrium. In this step, **C** is solvated by the 1-hexene bath, and the hydrogen atom that is bound to the metal center moves to the γ-carbon on the 1-hexene. After equilibrium has been established between **C** and **D₁**, **C** is again solvated by a 1-hexene molecule in ca. 150 μs. In this step, species **C** reacts to form $Fe(CO)_3(\eta^2\text{-1-hexene})(\eta^2\text{-2-hexene})$ (**D₂**): the hydrogen atom that is bound to the metal center moves to the α-carbon and the double bond migrates to the secondary position. Species **D₂** is 10 kcal/mol more stable than **C**, and therefore, the **C→D₂** reaction is irreversible, heavily favoring **D₂**. To complete the catalytic cycle, the 2-hexene ligand is dissociated from **D₂** to form either **B₁** or **C**; however, we do not observe this step since it is expected to occur on a longer time-scale than we can investigate with this experiment.[13,14]

The motivation for this work was to determine why photoactivated iron-carbonyl complexes are such extraordinary alkene-isomerization catalysts. Many authors have proposed that the efficiency of the reaction is linked to the high spin state of **B₁** since the turnover rate for the reaction catalyzed with photoactivated $Ru(CO)_5$, a complex with only singlet transient species in the catalytic cycle, is much less efficient.[8,11,16,17,19,22] However, this work indicates that the triplet form of **B₁** does not play a

17

significant role in the isomerization reaction since it reacts to form a singlet form of $\mathbf{B_1}$ on a sub-picosecond time-scale. The singlet form of $\mathbf{B_1}$ is a internally solvated structure with an agostic M–H–C bond that stabilizes the structure so that it is stable on the pico- through early nanosecond time-scale.[11] As a result, $\mathbf{B_1}$ selectively reacts to form $\mathbf{C}$ and is not solvated to form $\mathbf{D_1}$. This selectivity allows the alkene-isomerization reaction to proceed through $\mathbf{C}$ so that *both bisalkene isomers*, $\mathbf{D_1}$ and $\mathbf{D_2}$, are formed. Species $\mathbf{D_1}$ is not thermodynamically stable, and as a result, is a side-product in the reaction. On the other hand, the desired product, $\mathbf{D_2}$, is thermodynamically stable, and as a result the majority of the population of species $\mathbf{C}$ will ultimately react to form $\mathbf{D_2}$. When the system comes to equilibrium, nearly 100% of the alkene population will be 2-hexene.[3]

## ACKNOWLEDGMENT.

## SUPPORTING INFORMATION PARAGRAPH

Supporting information includes the following: (1) expanded step-scan FTIR data of $Fe(CO)_4$(1-hexene) in neat 1-hexene solution including discussion of experimental artifacts (2) Cartesian coordinates for DFT-calculated species and transition states (3) partial optimization calculations of the $^3\mathbf{B_1}\rightarrow\mathbf{C}$ performed with a B3LYP functional (4) partial optimization calculations with different starting structures of $^3\mathbf{B_1}$. This material is available free of charge via the Internet at http://pubs.acs.org.

REFERENCES.

1.    Crabtree, R.H., *The Organometallic Chemistry of Transition Metals*, John Wiley & Sons: New York, NY, 2001.

2.    Barrett, A.G., D.H. Barton, and G. Johnson, *J.C.S. Perkin Trans.* **1978**. 1, 1014.

3.    Fleckner, H., F.W. Grevels, and D. Hess, *Journal of the American Chemical Society* **1984**. 106, 2027.

4.    Gree, R., *Synthesis* **1989**. 5, 341.

5.    Knolker, H.J., A. Braier, D.J. Brocher, S. Cammerer, W. Frohner, P. Gonser, H. Hermann, D. Herzberg, K.R. Reddy, and G. Rohde, *Pure Appl. Chem.* **2001**. 73, 1075.

6.    Pearson, A.J., *Accounts of Chemical Research* **1980**. 13, 463.

7.    Rodreiguez, J., P. Brun, and B. Waegell, *Tetrahedron Lett.* **1986**. 27, 835.

8.    Barnhart, T.M., J. De Felippis, and R.J. McMahon, *Angew. Chem. Int. Ed. Engl.* **1993**. 32, 1073-1074.

9.    Barnhart, T.M. and R.J. McMahon, *Journal of the American Chemical Society* **1992**. 114, 5434.

10.   Ellerhorst, G., W. Gerhartz, and F.W. Grevels, *Inorg. Chem.* **1980**. 19, 67.

11.   Glascoe, E.A., K.R. Sawyer, J.E. Shanoski, and C.B. Harris, *Journal of Physical Chemistry C* **2007**. 111, 8789-8795.

12.   Gravelle, S.J., L.J. van de Burgt, and E. Weitz, *Journal of Physical Chemistry* **1993**. 97, 5272.

13.   Long, G.T. and E. Weitz, *Journal of the American Chemical Society* **2000**. 122, 1431.

14.   Long, G.T., W. Wenhua, and E. Weitz, *Journal of the American Chemical Society* **1995**. 117, 12810.

15.  Mitchener, J.C. and M.S. Wrighton, *Journal of the American Chemical Society* **1982**. 105, 1065.

16.  Wuu, Y.M., J.G. Bentsen, C.G. Brinkley, and M.S. Wrighton, *Inorg. Chem.* **1987**. 26, 530-540.

17.  Wuu, Y.M., C. Zou, and M.S. Wrighton, *Inorg. Chem.* **1988**. 27, 3039 - 3044.

18.  Hayes, D.M. and E. Weitz, *J. Phys. Chem* **1991**. 95, 2723.

19.  Leadbeater, N., *Coord. Chem. Rev.* **1999**. 188, 35-70.

20.  Poliakoff, M. and J.J. Turner, *J. Chem. Soc. Dalton* **1974**. 20, 2276.

21.  Lee, C., W. Yang, and R.G. Parr, *Physical Review B* **1988**. 37, 785.

22.  Ziegler, T., *Inorg. Chem.* **1986**. 25, 2721.

23.  Snee, P.T., C.K. Payne, S.D. Mebane, K.T. Kotz, and C.B. Harris, *Journal of the American Chemical Society* **2001**. 123, 6909.

24.  Scott, A.P. and L. Radom, *Journal of Physical Chemistry* **1996**. 100, 16502.

25.  Schroeder, M.A. and M.S. Wrighton, *Journal of the American Chemical Society* **1973**. 98, 551.

26.  Sun, H. and H. Frei, *Journal of Physical Chemistry B* **1997**. 101, 205-209.

27.  Yeom, Y. and H. Frei, *Journal of Physical Chemistry B* **2003**. 107, 6286-6291.

28.  Glascoe, E.A., M.F. Kling, J.E. Shanoski, R.A. DiStasio Jr., C.K. Payne, B.V. Mork, T.D. Tilley, and C.B. Harris, *Organometallics* **2007**. 26, 1424-1432.

29.  Niu, S. and M.B. Hall, *Chemistry Reviews* **2000**. 100, 353.

30.  Snee, P.T., C.K. Payne, K.T. Kotz, H. Yang, and C.B. Harris, *Journal of the American Chemical Society* **2001**. 123, 2255-2264.

31.   Snee, P.T., H. Yang, K.T. Kotz, C.K. Payne, and C.B. Harris, *Journal of Physical Chemistry A* **1999**. 103, 10426.

32.   Shanoski, J.E., E.A. Glascoe, and C.B. Harris, *Journal of Physical Chemistry B* **2006**. 110, 996-1005.

33.   Shanoski, J.E., C.K. Payne, M.F. Kling, E.A. Glascoe, and C.B. Harris, *Organometallics* **2005**. 24, 1852-1859.

34.   Cedeno, D.L. and E. Weitz, *Organometallics* **2003**. 22, 2652.

35.   Becke, A.D., *Physical Review A* **1988**. 38, 3098.

36.   Perdew, J.P., *Physical Review B* **1986**. 33, 8822.

37.   Francl, M.M., W.J. Petro, W.J. Hehre, J.S. Binkley, and J.A. Pople, *Journal of Chemical Physics* **1982**. 77, 3654.

38.   Hariharan, P.C. and J.A. Pople, *Theoretica Chimica Acta* **1973**. 28, 213.

39.   Hehre, W.J., R. Ditchfield, and J.A. Pople, *Journal of Chemical Physics* **1972**. 56, 2257.

40.   Hay, P.J. and W.R. Wadt, *Journal of Chemical Physics* **1985**. 82, 299-310.

41.   Peng, C.Y., P.Y. Ayala, H.B. Schlegel, and M.J. Frisch, *Journal of Computational Chemistry* **1996**. 17, 49.

42.   Peng, C.Y. and H.B. Schlegel, *Isr. J. Chem.* **1993**. 33, 449.

43.   Harvey, J.N., *Spin-Forbidden Reactions in Transition Metal Chemistry*, in *Computational Organometallic Chemistry*, T.R. Cundari, Editor. 2001, Marcel Dekker Inc.: New York, NY. p. 291-321.

44.   Becke, A.D., *Journal of Chemical Physics* **1993**. 98, 5648.

45.    Stephens, P.J., G.J. Devlin, C.F. Chabalowski, and M.M. Frisch, *Journal of Physical Chemistry* **1994**. 98, 11623.

46.    Ricca, A. and C.W. Bauschlicher, Jr., *Journal of Physical Chemistry* **1994**. 98, 12899.

47.    Wang, W. and E. Weitz, *Journal of Physical Chemistry A* **1997**. 101, 2358.

48.    Wong, M.W. and L. Radom, *Journal of Physical Chemistry* **1995**. 99, 8582.

49.    Bentsen, J.G. and M.S. Wrighton, *Journal of the American Chemical Society* **1987**. 109, 4530-4544.

50.    The average values for the two time constants were calculated by averaging each time constant for the two **D** peaks (1969 $cm^{-1}$ and 1977 $cm^{-1}$) and the two **C** peaks (1990 and 2058 $cm^{-1}$).

51.    The dynamics of the shoulder at 2045 $cm^{-1}$ are masked by the dynamics of the neighboring peak at 2058 $cm^{-1}$.

52.    Unpublished data

53.    Baesd on the amplitude of the 1930 $cm^{-1}$ peak, which is expected to be the largest peak in **E**, we expect the population of **E** to be small. Therefore, the contribution to the catalytic cycle will be small and not detectable.

54.    Desrosiers, M., D. Wink, R. Trautman, A. Friedman, and P. Ford, *Journal of the American Chemical Society* **1986**. 108, 1917.

55.    Bogdan, P.L. and E. Weitz, *Journal of the American Chemical Society* **1989**. 111, 3163.

56.    Poli, R. and J.N. Harvey, *Chemical Society Reviews* **2003**. 32, 1-8.

57.    Clot, E. and O. Einstein, *Principles and Applications of Density Functional Theory in Inorganic Chemistry II*, Springer: Berlin, Heidelberg, Germany, 2004.

58.  Yang, H., M.C. Asplund, K.T. Kotz, M.J. Wilken, H. Frei, and C.B. Harris, *Journal of the American Chemical Society* **1998**. 120, 10154-10165.

59.  Steinfield, J.I., J.S. Francisco, and W.L. Hase, *Chemical Kinetics and Dynamics*, Prentice-Hall Inc.: Upper Saddle River, NJ, 1999.

60.  By simple transition state theory we estimate that the barriers to forming the **C$_{mer}$** and **C$_{exo}$** isomers from **B$_2$** and **C$_{mer}$**, respectively, correspond to a time constant of ca. 200 ns.

61.  DFT geometry optimization and energy calculations have been performed for the cis-isomer of D$_2$ and indicated that this isomer is isoenergetic with the trans-isomer.

62.  If **D$_2$** is formed via the fast pathway, rate equations can be simplified to

$$\frac{d[C]}{dt} = k_2[C]$$

and

$$\frac{d[D]}{dt} = k_2[C].$$

Here the **D$_1$** to **C** back reaction can be neglected because the $k_2 \gg k_{-1}$ according to the DFT results summarized in Table 2.

63.  Cotton, F.A., G. Wilkinson, and P.L. Gaus, *Basic Inorganic Chemistry*, John Wiley and Sons: Toronto, 1995.

64.  Dougherty, T.P. and E.J. Heilweil, *Journal of Chemical Physics* **1994**. 100, 4006-4009.

65.  Previous studies have been performed with complexes with a pentene ligand, but the experiments presented herein have been performed with a hexene ligand.

66. The time constants reported in the main text are average values while the time constants in the figure are for the specific **C** and **D** peaks displayed.

**Table 1.** Dynamics of photoproducts of $Fe(CO)_4(\eta^2$-1-hexene) (**A**) in neat 1-hexene solution observed by time-resolved IR spectroscopy

| Species | Exp. Freq $(cm^{-1})$ | Lit. Freq $(cm^{-1})$ [11,16] | DFT Freq $(cm^{-1})$ | $\tau$ $(\mu s)$ | Trend |
|---|---|---|---|---|---|
| $Fe(CO)_4(\eta^2$-hexene) (**A**)[a] | 1977 | 1981 | 1986 | $28 \pm 6$ | rise |
| | | | | $170 \pm 45$ | rise |
| | 2000 | 2002 | 1996 | no change | |
| | 2078 | 2083 | 2003 | no change | |
| $Fe(CO)_3(\eta^2$-1-hexene) (**B₁**) | N/A | 1932 | 1960/72 ($S_0$) | no change | |
| | | | 1946/51 ($T_1$) | | |
| | N/A | 2031 | 2029 ($S_0$) | no change | |
| | | | 2009 ($T_1$) | | |
| $HFe(CO)_3(\eta^3$-$C_6H_9)$ (**C**)[b] | 1990 | 1994 | 1988/91 | $19 \pm 2$ | decay |
| | | | | $145 \pm 4$ | decay |
| | obscured by **A** | 2003 | | N/A | |
| | 2058 | 2060 | 2045 | $12 \pm 2$ | decay |
| | | | | $130 \pm 10$ | decay |
| $Fe(CO)_3(\eta^2$-hexene)$_2$ (**D**)[a, c, d] | 1969 | 1972 | 1963/60 | $20 \pm 2$ | rise |
| | | | | $141 \pm 5$ | rise |
| | obscured by **A** | 1977 | 1974/75 | refer to **A** | |
| | 2045 | 2048 | 2033/30 | obscured by **C** | |
| $Fe(CO)_3(\eta^2$-hexene)(alkyl) (**E**) | 1930 | N/A | N/A | no change | |

[a] The literature frequencies of **A** and **D** are estimated from $Fe(CO)_4(\eta^2$-1-pentene) and $Fe(CO)_3$(pentene)$_2$, respectively; [b] The DFT calculated CO stretching modes of $HFe(CO)_3(\eta^3$-$C_6H_9)$ correspond to the **C$_{endo}$** isomer. The DFT calculated CO stretching modes for the **C$_{exo}$** isomer are at 1987, 1993 and 2046 $cm^{-1}$. The analogous modes for the **C$_{mer}$** isomer are at 1978, 1983 and 2042 $cm^{-1}$. [c] The dynamics of the 1977 $cm^{-1}$ bleach are attributed to an overlapping **D** peak centered at 1977 $cm^{-1}$; [d] The first set of DFT calculated CO stretching frequencies correspond to the **D₁** isomer and the second set correspond to the **D₂** isomer.

**Table 2.** Relative energy and enthalpy of the key intermediates in the iron-assisted alkene isomerization reaction scaled relative to lowest energy isomer of $^3B_1$.

| Species | E (kcal/mol) | H (kcal/mol) |
|---|---|---|
| $B_1$* | 0.880 | -0.156 |
| $B_2$ | -8.82 | -9.68 |
| $B_1$ | -8.25 | -9.21 |
| $D_1$ | -9.15 | -10.5 |
| $C_{endo}$ | -11.2 | -12.8 |
| $C_{exo}$ | -12.2 | -13.2 |
| $C_{mer}$ | -8.86 | -9.73 |
| $D_2$ | -21.3 | -22.7 |
| $B_1 \rightarrow C_{exo}$ TS | 8.69 | 7.44 |
| $B_2 \rightarrow C_{exo}$ TS | 8.39 | 6.90 |
| $B_2 \rightarrow C_{mer}$ TS | -0.34 | -1.37 |
| $C_{endo} \rightarrow C_{mer}$ TS | -0.73 | -1.71 |
| $C_{mer} \rightarrow C_{exo}$ TS | -0.52 | -1.72 |
| $B_1 \rightarrow C_{endo}$ TS | -4.58 | -5.74 |
| $B_2 \rightarrow C_{endo}$ TS | -4.28 | -5.99 |

**Table 3.** Calculated structural parameters for key intermediates in the iron-assisted alkene isomerization reaction

| Species | Fe-αC | Fe-βC | Fe-γC | Fe-γH | Fe-αH |
|---------|-------|-------|-------|-------|-------|
| $^3B_1$ | 2.15 | 2.37 | 3.29 | 3.35 | 2.63 |
| $B_1$* | 2.04 | 2.04 | 3.16 | 3.35 | 2.71 |
| $B_1$ | 2.11 | 1.98 | 2.28 | 1.77 | 2.68 |
| $B_2$ | 2.25 | 1.99 | 2.17 | 2.67 | 1.78 |
| $C_{endo}$ | 2.15 | 2.09 | 2.22 | 1.52 | 2.65 |
| $C_{exo}$ | 2.15 | 2.08 | 2.22 | 1.52 | 2.68 |
| $C_{mer}$ | 2.14 | 2.08 | 2.25 | 2.65 | 1.50 |
| $D_1$ | 2.14 | 2.18 | 3.22 | 3.35 | 2.74 |
| $D_2$ | 3.17 | 2.18 | 2.17 | 2.70 | 3.43 |

**Scheme 1.** Proposed mechanism for pentene isomerization catalyzed by photoactivated $Fe(CO)_5$ based on time-resolved studies performed in the gas phase.[65]
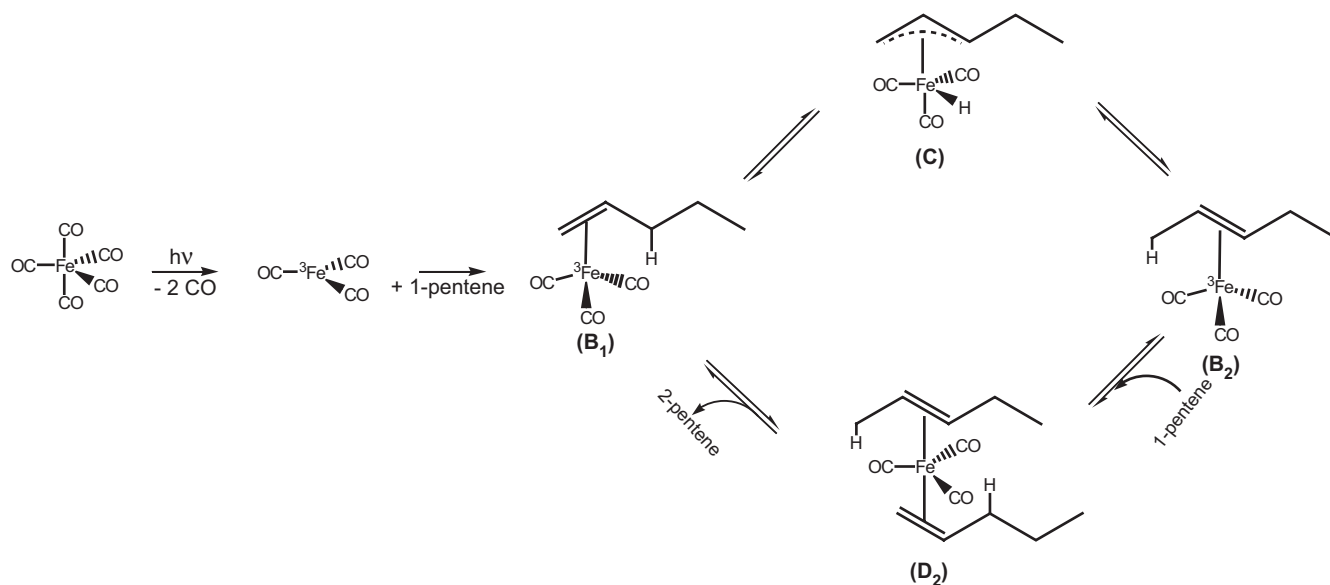


**Scheme 2.** 1,3-hydrogen migration in $Fe(CO)_3(\eta^2\text{-alkene})$ (**B**) through allyl hydride intermediates (**C**). The barrier to each step is listed in units of kcal/mol. The **B→C$_{endo}$** reactions (**B** = **B$_1$** and/or **B$_2$**) are not expected to be relevant since the barriers to these reactions are an order of magnitude higher than the barriers to the reactions shown here.
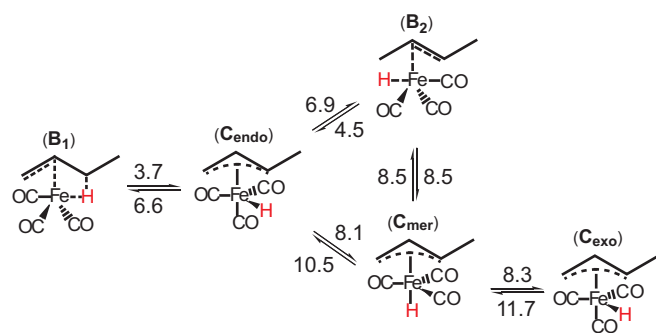
**Scheme 3.** Summary of time-resolved IR studies of Fe(CO)$_4$($\eta^2$-1-hexene) in neat 1-hexene solution on the pico- through the microsecond time-scales. Note that we cannot rule out the possibility that there are short-lived intermediates to the **C→D** reactions and cannot establish the role of the different **C** in the **C→D** reaction.
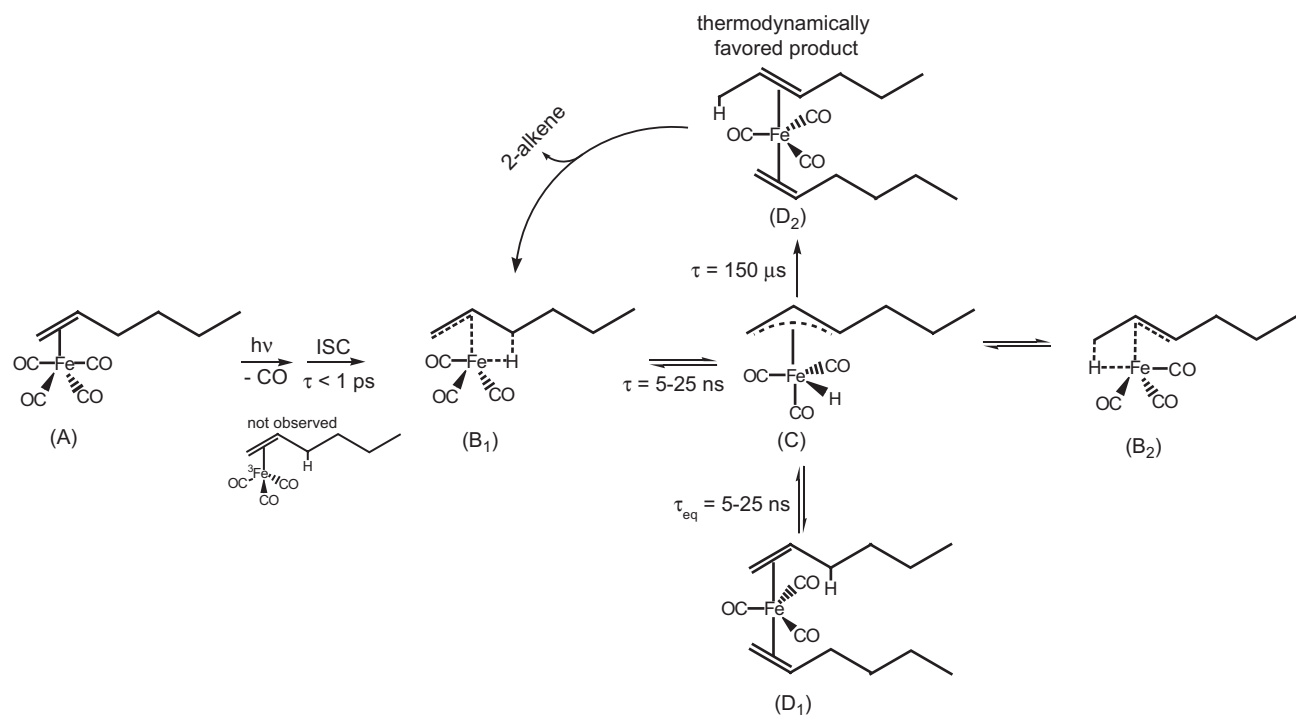
**Figure 1.** Transient IR spectra of Fe(CO)$_4$($\eta^2$-1-hexene) (**A**) in solution with neat 1-hexene on the (a) nanosecond and (b) microsecond time-scales. The oscillations marked with '*' are experimental artifacts and are discussed further in SI.
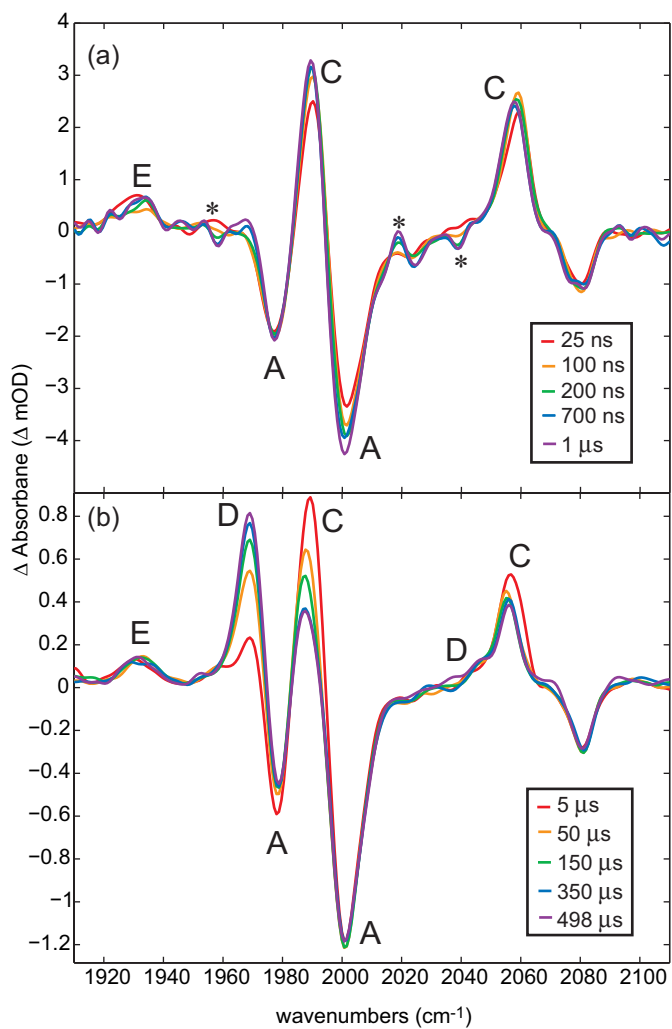
**Figure 2.** Kinetic trace of the 1990 cm$^{-1}$ peak (**C**) and the 1969 cm$^{-1}$ (**D**) [66]



(a) 2058 cm$^{-1}$ peak (**C**)
HFe(CO)$_3$($\eta^3$-C$_6$H$_9$)

$\tau_{rise}$ = 20 ± 2 µs and 141 ± 5 µs

(b) 1969 cm$^{-1}$ peak (**D**)
Fe(CO)3($\eta^2$-hexene)$_2$

$\tau_{decay}$ = 12 ± 2 µs and 130 ± 10 µs

∘ experimental data
—— biexponential (scenario 1)
– – single exponential (scenario 2)

Δ Absorbane (Δ mOD)

time (µs)
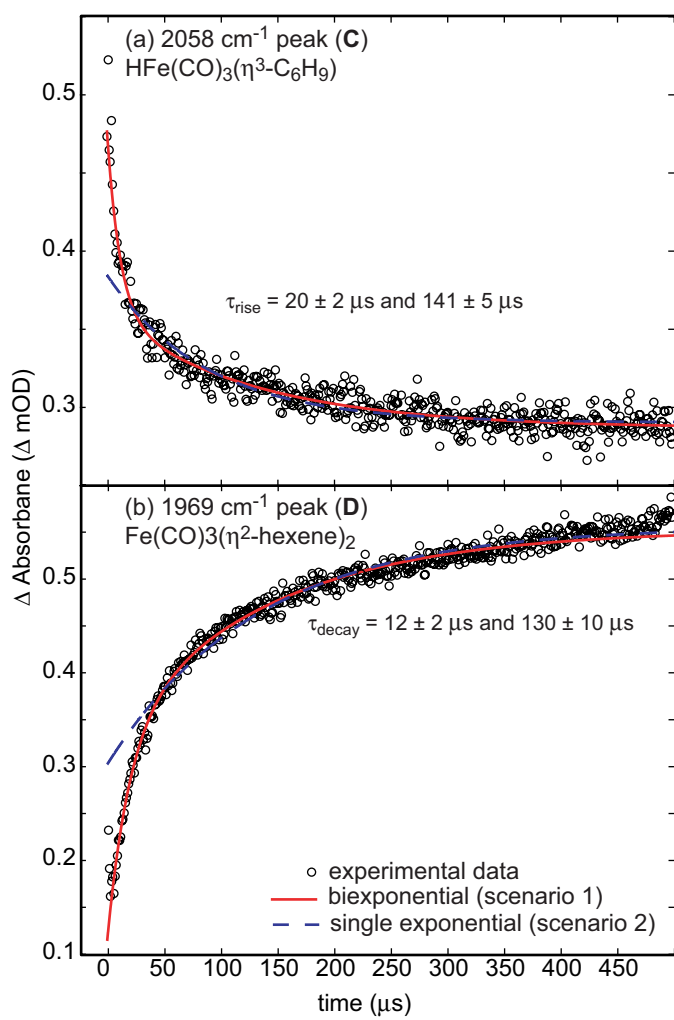
**Figure 3.** DFT calculated one-dimensional potential energy surfaces of the ground singlet and triplet spin states ($S_0$ and $T_1$) of $Fe(CO)_3$(1-butene) along the Fe–$\gamma$H bond. The curves are generated by performing successive partial geometry optimizations at fixed values of the Fe–$\gamma$H distance. The lines that connect the data points are guides to the eye. The dashed line on the $S_0$ potential at 3 Å corresponds to a small shift in the position of the CO ligands and is not physically meaningful.
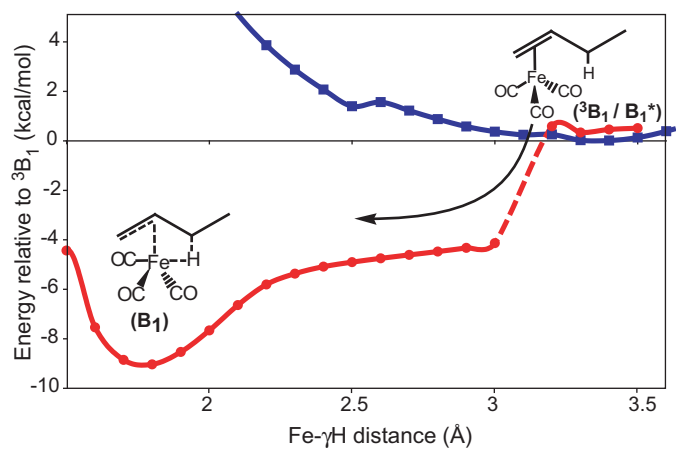
**Figure 4.** DFT calculated structures of (a) $^3Fe(CO)_3(\eta^2$-1-butene) ($^3\mathbf{B_1}$), (b) $^1Fe(CO)_3(\eta^2$-1-butene) ($\mathbf{B_1^*}$), (c) $^1Fe(CO)_3(\eta^2$-1-butene) with a M–γH–C agostic interaction ($\mathbf{B_1}$), (d) $^1Fe(CO)_3(\eta^2$-2-butene) ($\mathbf{B_2}$) with a M–αH–C agostic interaction, (e) facial-endo $HFe(CO)_3(\eta^3$-$C_4H_7$) ($\mathbf{C_{endo}}$), (f) facial-exo $HFe(CO)_3(\eta^3$-$C_4H_7$), (g) meridional $HFe(CO)_3(\eta^3$-$C_4H_7$). The energies listed are relative to the lowest energy structure of $^3\mathbf{B_1}$. Below each DFT structure is the analogous structure observed in the experiments (i.e. with a hexene ligand).

DFT-generated structure of Fe(CO)$_3$($\eta^2$-alkene)
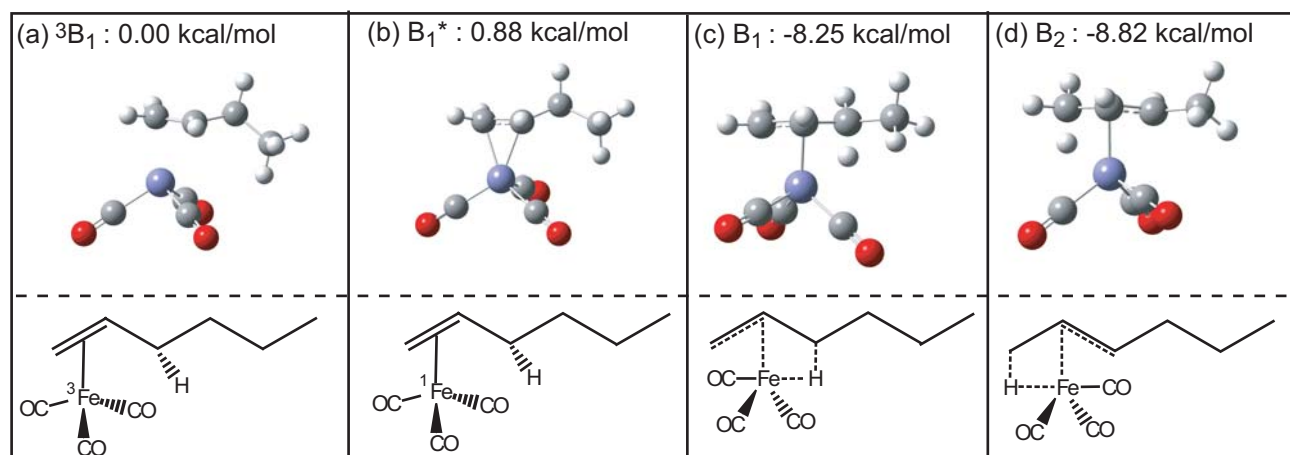


DFT-generated structure of Fe(CO)$_3$($\eta^3$-allyl)



◯ = Fe  ◯ = C  ◯ = O  ◯ = H
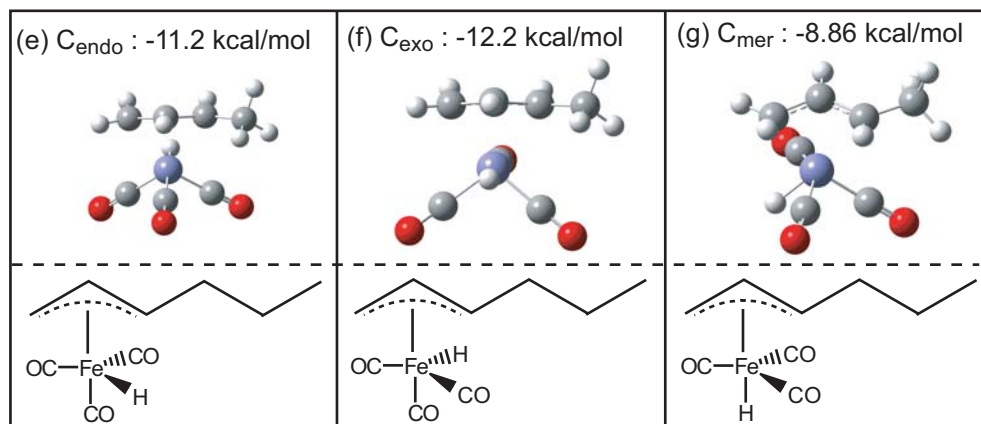
**Figure 5.** DFT calculated relative energies of species **C**, **D₁** and **D₂** and the energetic barriers that connect them as determined by the time-resolved IR experiments. The energies of all minima and transition states are scaled relative to the lowest energy structure of $^3Fe(CO)_3(\eta^2$-1-alkene) ($^3\mathbf{B_1}$).
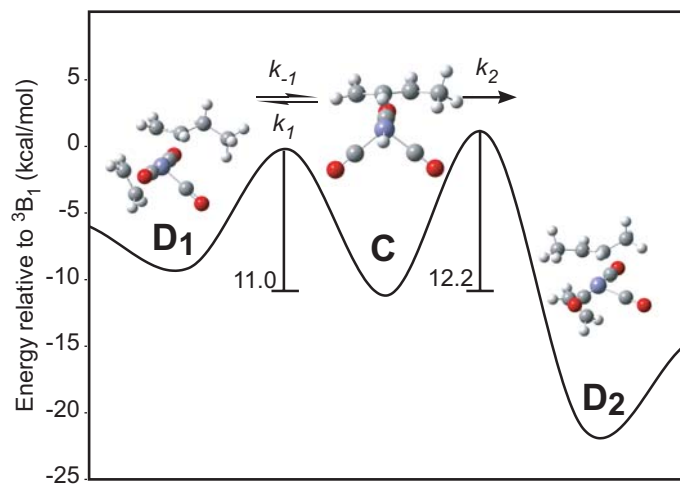
UV-photolysis of $Fe(CO)_4(\eta^2$-1-hexene) leads to the dissociation of a CO to form singlet form of $Fe(CO)_3(\eta^2$-1-hexene). This compound rearranges to form an allyl hydride in 5–25 ns, but does not coordinate a hexene molecule. We observe the coordination of the alkene ligand to the allyl hydride, leading to the formation of the bis-alkene isomers, $Fe(CO)_3(\eta^2$-1-hexene)$(\eta^2$-2-hexene) and $Fe(CO)_3(\eta^2$-1-hexene)$_2$. The efficiency of the isomerization is attributed to the thermodynamic stability of $Fe(CO)_3(\eta^2$-1-hexene)$(\eta^2$-2-hexene) over $Fe(CO)_3(\eta^2$-1-hexene)$_2$.